

Quantitative SPECT reconstruction using CT-derived corrections

Kathy Willowson^{1,2}, Dale L Bailey^{1,2,3} and Clive Baldock¹

¹ Institute of Medical Physics, School of Physics, University of Sydney, Camperdown, NSW 2006, Australia

² Department of Nuclear Medicine, Royal North Shore Hospital, St Leonards, NSW 2065, Australia

³ Faculty of Medicine and Discipline of Medical Radiation Sciences, Faculties of Health, University of Sydney, Lidcombe, NSW 2141, Australia

E-mail: K.Willowson@physics.usyd.edu.au

Received 24 January 2008, in final form 25 March 2008

Published 21 May 2008

Online at stacks.iop.org/PMB/53/3099

Abstract

A method for achieving quantitative single-photon emission computed tomography (SPECT) based upon corrections derived from x-ray computed tomography (CT) data is presented. A CT-derived attenuation map is used to perform transmission-dependent scatter correction (TDSC) in conjunction with non-uniform attenuation correction. The original CT data are also utilized to correct for partial volume effects in small volumes of interest. The accuracy of the quantitative technique has been evaluated with phantom experiments and clinical lung ventilation/perfusion SPECT/CT studies. A comparison of calculated values with the known total activities and concentrations in a mixed-material cylindrical phantom, and in liver and cardiac inserts within an anthropomorphic torso phantom, produced accurate results. The total activity in corrected ventilation-subtracted perfusion images was compared to the calibrated injected dose of [^{99m}Tc]-MAA (macro-aggregated albumin). The average difference over 12 studies between the known and calculated activities was found to be -1% , with a range of $\pm 7\%$.

(Some figures in this article are in colour only in the electronic version)

1. Introduction

In quantitative single-photon emission computed tomography (SPECT), the calculation of absolute radionuclide concentrations allows useful information to be obtained regarding *in vivo* function. Such data have not been readily available from SPECT studies, due primarily to the degrading effects of attenuated and scattered photons. In addition, quantitative values from structures that have a diameter less than approximately three times the total system

spatial resolution can also be affected by the partial volume effect (Hoffman *et al* 1979). X-ray computed tomography (CT) has previously been used as an accurate tool to perform patient-specific, non-uniform attenuation correction (Moore 1982, LaCroix *et al* 1994, Blankespoor *et al* 1996, Kashiwagi *et al* 2002). This method relies on the use of an attenuation (μ) map which is created from the CT data using a conversion from Hounsfield units to attenuation coefficients. This approach to attenuation correction has become highly practical with the introduction of combined SPECT/CT systems, and offers the additional benefit of fusing high-resolution anatomical images together with functional images (Bocher *et al* 2000, Roach and Bailey 2005).

Scattered photons have a significant degrading impact on image quality and, in particular, affect image contrast and the relationship between source activity and image intensity. In general, about 30–40% of photons detected in the photo-peak have been scattered at least once when imaging with ^{99m}Tc (Buvat *et al* 1994). These scattered photons lead to inaccurate results if a suitable scatter correction technique is not used. The accuracy of the transmission-dependent scatter correction (TDSC) method (Meikle *et al* 1994) has been previously demonstrated (Meikle *et al* 1994, Narita *et al* 1996, Vines *et al* 2003). Briefly, the method is based on estimating scatter by the convolution of the photo-peak image with a suitable scattering kernel followed by subtraction (Axelsson *et al* 1984), and uses transmission data supplied from an additional transmission scan to calculate a scatter fraction on a pixel-by-pixel basis, as opposed to a global scatter fraction (Meikle *et al* 1994). As such, transmission information derived from CT data can potentially be used to perform both non-uniform attenuation *and* scatter corrections, using the TDSC technique. Larsson *et al* (2003) investigated the use of x-ray CT data to perform attenuation and scatter corrections on brain SPECT studies using Monte Carlo simulations. It was found that TDSC in conjunction with CT-based attenuation correction could offer a practical technique for deriving quantitative results. However, the study did not investigate additional corrections such as partial volume effect correction, system dead time correction and did not validate quantitative accuracy on patient data. A further investigation of quantitative SPECT using x-ray CT corrections was carried out by Vandervoort *et al* (2007), who demonstrated the use of an iterative scatter correction method in conjunction with attenuation correction when analyzing ^{99m}Tc myocardial SPECT studies. The study demonstrated that quantitative accuracy was the best when using CT-derived transmission maps, as opposed to a separate radionuclide transmission scan, hinting at the role that CT is destined to play in quantitative analysis for SPECT/CT systems. However, to our knowledge, no study to date has investigated a suitable CT-based quantitative technique for ^{99m}Tc clinical studies in general, and further, the evidence of quantitative accuracy in real patient data is required.

The aim of this study is to develop a comprehensive quantitative method using CT-derived corrections for attenuation and scatter, and the partial volume effect (where necessary), validated in the clinical setting. A method has been developed that uses measurements of camera sensitivity and response to dead time to improve the accuracy of quantitative values from SPECT images and to produce images in the units of absolute activity (kBq cm^{-3}). Such corrections are camera/collimator-specific and depend on the choice of radionuclide.

2. Methods

All experimental data were acquired with a SKYLight dual-head SPECT system (Philips Medical Systems, North Milpitas, CA, USA) of crystal thickness 16 mm, which was integrated with a single slice Picker PQ5000 helical CT scanner (Bailey *et al* 2007). Vertex general purpose (VXGP) parallel-hole collimators were used, with hole size 1.78 mm, hole length

42.0 mm, septal thickness 0.152 mm and 7.8 mm system full-width-at-half-maximum (FWHM) at 10 cm. All images were acquired using ^{99m}Tc with a 20% symmetric energy window centered on 140 keV.

2.1. Transmission-dependent scatter correction

TDSC is based on the convolution-subtraction model (Axelsson *et al* 1984, Msaki *et al* 1987), such that the scatter component of the image (g_s) is estimated by convolving the observed projection data (g_{obs}) with a scatter function (s):

$$\hat{g}_s = k(g_{\text{obs}} \otimes s) \quad (1)$$

where the scatter fraction (k) scales the convolution to give the correct amount of scatter, which can then be subtracted from the observed projection data.

The scatter function (s) represents the response of a position-sensitive detector to scattered radiation, which cannot be discriminated from the photo-peak due to the limited energy resolution of the camera. The scatter function is generally evaluated by determining the response of the imaging system to a line source and modeled as a decreasing mono-exponential (Axelsson *et al* 1984, Msaki *et al* 1993, Meikle *et al* 1994, Kim *et al* 2003), or as a combination of a Gaussian plus exponential (Narita *et al* 1996).

An iterative approach to scatter correction was introduced by Bailey *et al* (1988), where the estimate of scatter is successively updated based on the corrected data calculated at each previous step. Ljungberg and Strand (1991) demonstrated with Monte Carlo simulations that the scatter distribution is highly dependent on a particular object's density and geometry, leading to the introduction of a variable scatter fraction calculated for every point in the projection data based on radionuclide-source-based transmission map measurements (Bailey *et al* 1987, Mukai *et al* 1988, Ljungberg and Strand 1990, Meikle *et al* 1994). These pixel-by-pixel-based scatter fractions can be calculated from transmission data acquired simultaneously with the emission study, or from ray sums through an attenuation map obtained from an alternative imaging modality, such as CT. Using the notation in (1), the TDSC method can then be expressed as

$$\hat{g}(x, y) = g_{\text{obs}}(x, y) - k(x, y)(g_{\text{obs}}(x, y) \otimes s) \quad (2)$$

where $\hat{g}(x, y)$ is the estimated scatter-corrected image and $k(x, y)$ is the matrix of scatter fractions derived from the transmission data. Scatter fractions can be calculated using empirical constants that represent the build-up function of the system (Wu and Siegel 1984, Siegel *et al* 1984). Siegel *et al* derived a generalized build-up function for geometric mean images which describes the build up for a given attenuation path length μd :

$$A - B e^{-\mu d \beta} \quad (3)$$

As demonstrated by Meikle *et al* (1994), if the geometric mean of conjugate views is taken, the scatter fraction per pixel can be written in terms of the measured transmission ($e^{-\mu T}$), and can be related to the build-up function as

$$k = 1 - \frac{1}{A - B(e^{-\mu T})^{\beta/2}} \quad (4)$$

The exponential term $e^{-\mu T}$ is equivalent to the transmission factor at a point, and can hence be measured from transmission data. The constants A , B and β must be experimentally determined. The relationship is now expressed in terms of the total thickness T , as opposed to the depth d , which accounts for the factor of 1/2 in the exponent.

The scatter function for the Philips SKYLIGHT was modeled as a mono-exponential function, the slope of which was determined by experiments on a line source in a tank of

water. The accuracy of the calculated scatter function was assessed by comparing the full-width-at-tenth-maximum (FWTM) of a scatter-free profile from a line source imaged in air to the FWTM of the scatter-corrected profile from the line source imaged in water.

As described by Meikle *et al* (1994), the build-up function of the system was modeled by acquiring images of a flood source through varying depths of water (0–16 cm), keeping the source-to-detector distance constant. Broad beam measurements (C_{broad}) were taken as the count rate observed from the field-of-view corresponding to the area of the Perspex tank. The equivalent narrow beam counts (C_{narrow}) were calculated at each depth by applying the known narrow beam attenuation coefficient for water (0.145 cm^{-1}) to the measurement made in air. The scatter fraction for each measurement was then calculated as

$$k = \frac{C_{\text{broad}} - C_{\text{narrow}}}{C_{\text{broad}}} \quad (5)$$

Equation (4) was fitted to a plot of calculated transmission values against scatter fraction values, giving rise to the necessary constants.

2.2. Measuring the camera sensitivity factor

The camera sensitivity factor is effectively a measure of how many counts the gamma camera detects for every unit of radioactivity in the field-of-view, and is a necessary parameter to allow for the conversion between the count rate and units of absolute activity. As such, the sensitivity of a gamma camera is detector thickness, collimator and radionuclide dependent. To measure the sensitivity, a small calibrated amount of $^{99\text{m}}\text{Tc}$ was imaged in a paper cup (low attenuating) equidistant from both heads. Care was taken to ensure that the camera dead time and photon attenuation were not significant. A static study without any source present was also acquired so that any background counts could be subtracted. The sensitivity in the units of counts $\text{s}^{-1} \text{ MBq}^{-1}$ was then derived from the count rate and the known amount of radioactivity.

2.3. Modeling the partial volume effect and the system recovery coefficient

Due to the partial volume effect, objects less than approximately three times the resolution of the system appear to contain lower concentrations of radioactivity than the actual value (Hoffman *et al* 1979). Correction for the partial volume effect involves the calculation of the recovery coefficient, which represents the ratio of the apparent concentration to the true concentration. A recovery coefficient correction factor can be applied to correct for the underestimation of concentrations for small objects if the size of the object can be measured, for example, from a CT study (Thomas *et al* 2005).

To determine the recovery coefficient of the Philips SKYLIGHT, several SPECT/CT studies were performed on cylinders of varying diameters, each containing a known concentration of activity. The diameter of the cylinders ranged from 5 mm to 21 cm, including sizes below the known spatial resolution of the system and others well above. The spatially co-registered CT studies were used to draw regions of interest (ROIs) corresponding to a cross-section through each cylinder. The observed activity in each region of the SPECT reconstructions was compared to the known activity inside the cylinders at the time of scanning, allowing the calculation of the recovery coefficient and the modeling of the system's partial volume effect.

2.4. Dead time

Although system dead time plays a significant role only when large amounts of radioactivity are present, it is desirable to take such a loss of counts into consideration to obtain quantitative

data. A dynamic 48 h acquisition was performed on a cylindrical phantom filled uniformly with ^{99m}Tc in water. The acquisition was divided into 288 separate 10 min frames. A relationship between the observed count rate and the true count rate was found by extrapolating the linear trend seen at low count rates, when dead time effects are negligible. The cascaded paralyzable–non-paralyzable dead time model (Cranley *et al* 1980, Bailey 1998) was fitted to the data using the equation

$$r' = \frac{r}{e^{(r\tau_p)} + ((\tau_{\text{NP}}/\tau_p) - 1)r\tau_p} \quad (6)$$

where r' is the observed count rate, r is the true count rate, τ_p is the paralyzable component of the system dead time and τ_{NP} is the non-paralyzable component, both of which are system-dependent parameters expressed in micro-seconds (μs). The relationship between the true count rate and the observed count rate was used to create a lookup table which allowed the percentage of count loss due to dead time for a given observed count rate to be calculated. The dead time correction factor described as a percentage of the total observed count rate for the study could then be applied to the reconstructions.

2.5. Quantitative reconstruction process and algorithm

A procedure was written in IDL (ITT, Boulder, Colorado) to perform TDSC on the SPECT acquisition data, given the spatially co-registered attenuation map, calculated from the CT data using the known conversion between Hounsfield and attenuation units (Brown *et al* 2008). The scatter-corrected projections were reconstructed using the standard Hermes (Nuclear Diagnostics AB, Stockholm) OSEM reconstruction package, with no filtering. The scatter-corrected SPECT data, the associated reconstructed data and the co-registered attenuation map were then passed to an iterative Chang attenuation correction algorithm written in IDL (Chang 1978), which performs the patient-specific attenuation correction based upon the CT-derived attenuation correction map (Manglos *et al* 1987). Previous studies have demonstrated that a single iteration of this algorithm was found to be sufficient, after which the change in the scatter- and attenuation-corrected images was considered insignificant (Bailey *et al* 1987). The resulting reconstructed scatter- and attenuation-corrected images were then corrected for any dead time loss before the pixel values were converted to activity units (kBq cm^{-3}) using the experimentally determined camera sensitivity factor and the duration of the acquisition. All data analysis and manipulation was carried out on a HERMES workstation.

2.6. Experimental validation

Two experiments were performed using phantoms to provide an initial validation of the quantitative method. The first experiment used a cylindrical phantom containing mixed materials (figure 1) to provide a variable and complex geometry of differing attenuation properties. The phantom contained 316 MBq of ^{99m}Tc mixed uniformly in water and the solid materials were kept non-radioactive. A 30 min SPECT study was acquired with 120 projections in a 128×128 matrix, followed by a CT study (beam current = 30 mA, tube voltage = 130 kV_p) which was used to derive an attenuation map.

The second phantom study was performed using an anthropomorphic torso phantom (Data Spectrum Corporation, Hillsborough, NC, USA) complete with inserts for the lungs, spine, heart and liver (figure 2). The ^{99m}Tc concentrations were 481 kBq ml⁻¹ in the liver compartment and 270 kBq ml⁻¹ in the inner chamber of the cardiac insert. The body cavity of the phantom contained a concentration of 0.6 kBq ml⁻¹ to represent a suitable level of

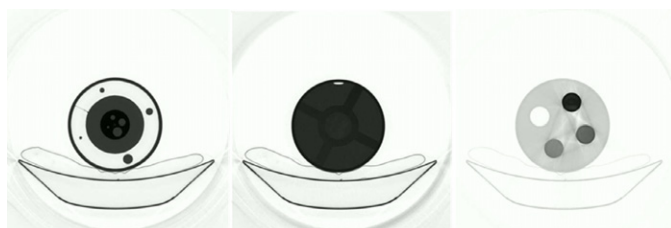


Figure 1. Three transverse slices from the x-ray CT of the mixed material phantom. The structure of the phantom is cylindrical, and the presence of materials with different attenuating properties can be seen.

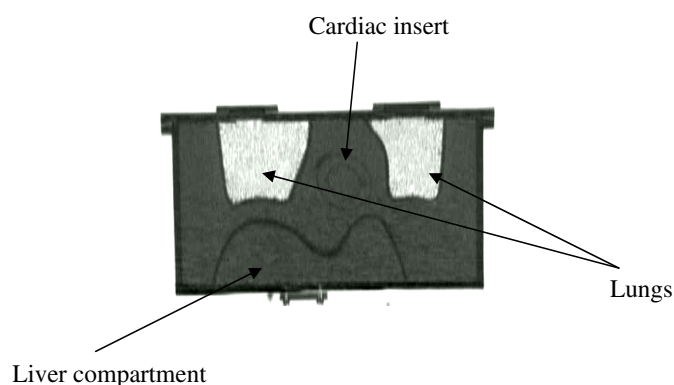


Figure 2. A single coronal slice from the resulting x-ray CT of the anthropomorphic torso phantom. The cardiac, liver and lung inserts are visible. The body of the phantom is filled with water, as are the cardiac and liver chambers, with specific concentrations of ^{99m}Tc . The lung chambers are filled with styrofoam beads and water to simulate the density of lung tissue.

background counts. The lungs and spine contained no activity. A 30 min SPECT study was acquired with 120 projections, followed by a CT study (30 mA, 130 kV_p).

Both phantom studies were reconstructed following the quantitative procedure described in section 2.5, and the images in absolute activity units were evaluated to compare the total activity at the time of the study (first phantom study) and the organ-specific concentrations (second phantom study), using the additional correction for the partial volume effect when analyzing the cardiac chamber (diameter = 35 mm).

2.7. Clinical validation

The clinical validation of the quantitative accuracy was evaluated in 12 lung ventilation/perfusion (V/Q) SPECT/CT patient studies. Each study consisted of a ventilation scan performed after the patient breathes in Technegas (Cyclomedica, Lucas Heights, Australia), followed by a perfusion scan where the patient is injected with a pre- and post-calibrated dose of [^{99m}Tc]-MAA (macro-aggregated albumin). A CT scan was used to provide attenuation data. Both the ventilation and perfusion studies were scatter- and attenuation-corrected in parallel, before the co-registered reconstructed ventilation data were subtracted after decay correction from the reconstructed perfusion data. The subtracted study then

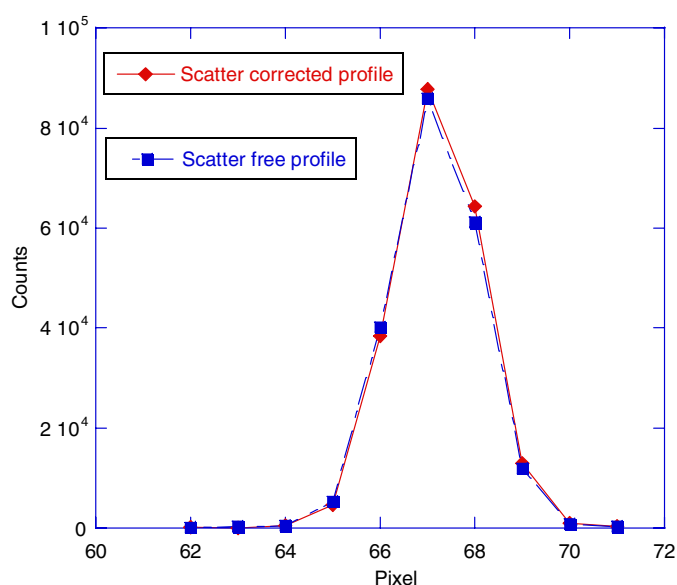


Figure 3. Comparison between the scatter-free profile taken from the line source imaged in air, and the scatter-corrected profile calculated from the line source imaged in water. This profile was scatter-corrected by subtracting the scattered counts that were estimated using the calculated scatter function. The data were also attenuation-corrected by applying the suitable attenuation coefficient of 140 keV in water, so that the profiles could be compared.

continued through the quantitative procedure described in section 2.5, such that the total activity of the transverse slices expressed in the units of MBq could be compared to the calibrated injected dose.

3. Results

3.1. Scatter function and scatter fraction parameters

The slope of the mono-exponential scatter function was calculated to be $(0.49 \pm 0.01) \text{ cm}^{-1}$. This scatter function was used to subtract the extrapolated scatter from the profile of the line source imaged in water, which had an approximate FWTM of $(2.79 \pm 0.5) \text{ cm}$, prior to scatter correction. The resulting scatter-subtracted profile is compared to the scatter-free profile from the line source imaged in air in figure 3, and was found to have a FWTM of $(1.88 \pm 0.02) \text{ cm}$, compared to the FWTM of the scatter-free profile equal to $(1.92 \pm 0.02) \text{ cm}$.

Figure 4 is the resulting plot of the data from the build-up experiment. The function described in equation (4) fitted the data with a root mean square value of 0.99, and the values of the constants A , B and β were found to be 1.95 ± 0.17 , 0.93 ± 0.17 and 0.31 ± 0.08 , respectively. It should be noted that the parameter B is equivalent to $(A - 1)$, a result that confirms the fact that the scatter fraction has a y-intercept of zero.

3.2. Sensitivity factor

Using the methods described previously, the sensitivity factor was found to be $(76.7 \pm 2.0) \text{ counts s}^{-1} \text{ MBq}^{-1}$ per detector head.

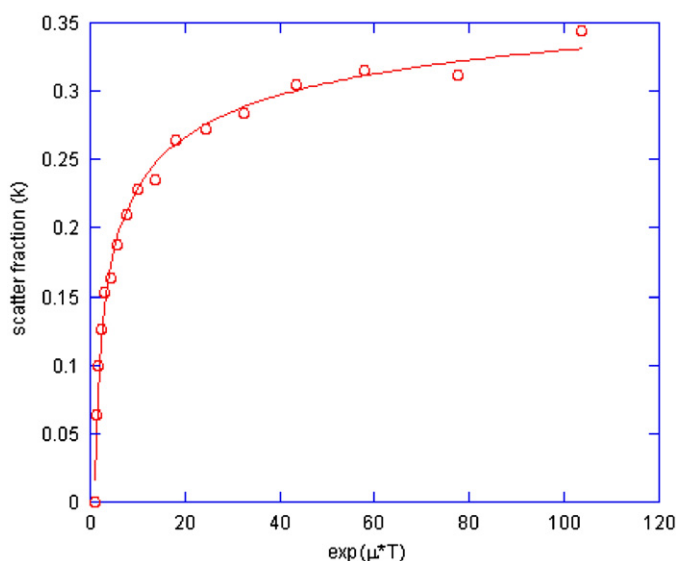


Figure 4. The resulting function (3) (solid line) fitted to the data (○) obtained from the ^{99m}Tc build-up experiment performed on the Philips SKYLIGHT. The empirical constants derived from the model allow the calculation of scatter fractions corresponding to transmission through a given thickness of attenuating material.

3.3. Recovery coefficient

Figure 5 is the plot of the calculated recovery coefficient against object diameter as a fraction of the system spatial resolution. A function of the form

$$y = 1 - a(e^{-bx}) \quad (7)$$

was fitted to the data with an R^2 -value of 0.94, to allow interpolation between the object sizes used. The plot provides the fraction of activity that is recovered from a reconstructed image of a small object with a given diameter, and so allows for the true concentration to be calculated.

3.4. System dead time

The relationship between the observed and true count rate is represented in figure 6. The paralyzable–non-paralyzable dead time function has been fitted to the data with an R^2 -value of 1.0, and the resulting parameters are used to create a lookup table of corrected count rates. This model allows the effects of dead time to be taken into account by estimating the true count rate which would be measured if no dead time effects were present for a specific measured count rate. The paralyzable and non-paralyzable components of the system dead time were found to be $(2.51 \pm 0.02) \mu\text{s}$ and $(1.15 \pm 0.01) \mu\text{s}$, respectively.

3.5. Experimental validation

The SPECT/CT study on the mixed material phantom was reconstructed following the quantitative reconstruction process (section 2.5). The sum of the reconstructed slices yielded a calculated total activity of $(309 \pm 15) \text{MBq}$ compared to the known injected, decay-corrected

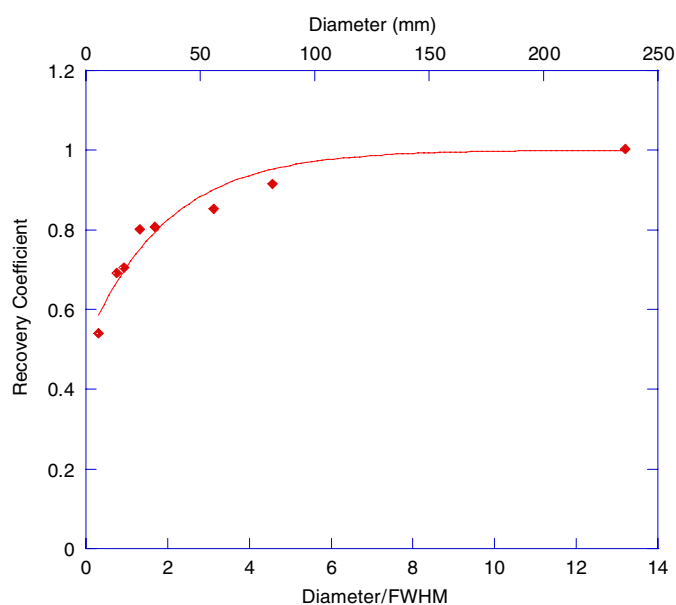


Figure 5. The plot of recovery coefficient values against object diameter as a fraction of the system spatial resolution, represented as the FWHM. It is not until objects are approximately three times the size of the system FWHM that they have a recovery coefficient of 1. The FWHM of the SKYLIGHT was measured as 15.9 mm.

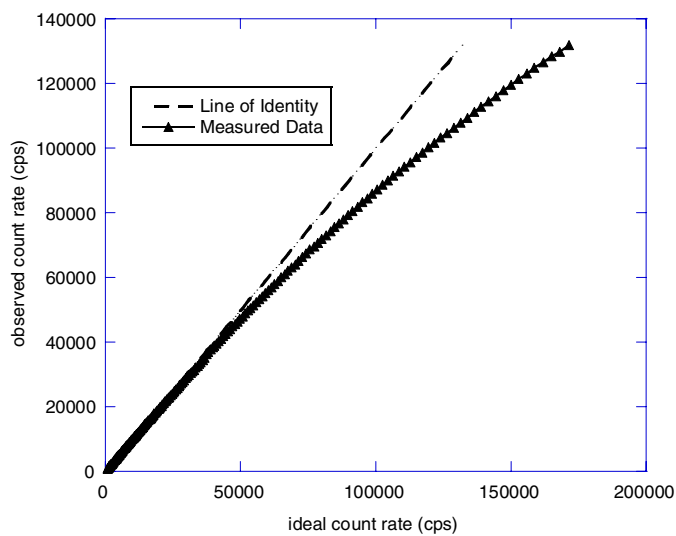


Figure 6. The paralyzable–non-paralyzable dead time model for the Philips SKYLIGHT. The function fitted to the measured data (6) provides a relationship between the true and observed count rates. Comparison with the line of identity demonstrates the effects of camera dead time for measured count rates of approximately 40 keps and above.

activity of 316 MBq at the mid-point of the acquisition. The average residual in cold spots was measured over several slices and was found to differ depending on the density of the

Table 1. Quantitative results from the clinical lung ventilation/perfusion studies. Each patient's ventilation (V) and perfusion (Q) study was scatter- and attenuation-corrected, before the decay-corrected V was subtracted from the Q . The subtracted studies were then dead-time-corrected before being converted to the units of absolute activity. The sum of the reconstructed slices yielded a total activity value (calculated dose), which was compared to the calibrated dose injected at the time of the study.

Patient no.	Calibrated dose (MBq)	Calculated dose (MBq)	Difference (%)
1	125	122	-2.4
2	109	106	-2.7
3	122	113	-7.4
4	137	131	-4.3
5	144	147	+2.1
6	165	168	+1.9
7	148	149	-0.7
8	134	131	-2.2
9	134	131	-2.2
10	134	139	+3.7
11	121	120	-0.7
12	135	134	-0.7

material. The measured cold spot residual as a percentage of background was found to vary between 0% and 13%, with the percentage value increasing as material density decreased. The highest residual measurement was found in air, which can be explained by the known phenomenon whereby reconstructed images in areas of no attenuation lead to erroneously high count densities and reduced contrast (Zaidi and Hasegawa 2003).

The anthropomorphic study was also evaluated with the quantitative reconstruction process, however, in this case the radioactivity concentration in the inner chamber of the cardiac insert and liver was calculated, as opposed to the total activity added to the phantom at the time of scanning. Several ROIs over different slices of the reconstructed quantitative image were analyzed to give an average value for the concentration in each organ. In addition, when analyzing the concentration in the inner chamber of the cardiac insert, the diameter of the chamber was measured from the CT image and used in conjunction with the results in figure 5 to determine the appropriate recovery coefficient factor. The average concentrations in the liver and inner chamber of the cardiac insert were calculated at (473 ± 24) kBq ml⁻¹ and (259 ± 13) kBq ml⁻¹, respectively (true values = 481 and 270 kBq ml⁻¹, respectively). The cardiac value was calculated with a recovery coefficient factor of 0.8, corresponding to an average measured diameter of 35 mm across the inner cardiac chamber from the CT.

3.6. Clinical validation

Table 1 represents the quantitative results from the clinical lung ventilation/perfusion studies. Over the 12 patient studies that were analyzed, the average difference between the calculated and true activities was found to be -1%, with a range of -7% to +4%. The error associated with the calibrated dose was calculated as ± 0.1 MBq, corresponding to the standard deviation in successive measurements made on the radionuclide dose calibrator. Also, as these were difference measures of the dose calibrated (pre-injection–post-injection), the absolute error would be expected to be very small.

4. Discussion

The agreement of the FWTM of the scatter-subtracted line source profile and the scatter-free line source profile to within a few percent supports the correct modeling of the scatter function. An uncertainty of only 1% was associated with the calculated slope of the scatter function and, as such, does not contribute largely to the overall uncertainty in the quantitative procedure.

The scatter fraction parameters calculated from the build-up experiment in figure 4 fitted the model well and are consistent with previous studies. The parameter B being equivalent to $(A - 1)$ is a further indication of this accuracy. The calculated values are in a similar range to other published values, such as Deloar's $A = 1.75$, $B = 0.75$ and $\beta = 0.53$ (Deloar *et al* 2004). The uncertainty associated with the parameter β is a large contributor to the total error involved in the quantitative process as it is an exponent in (3), the function used to calculate the scatter fraction for a given attenuation value.

The plot of the system recovery coefficient is as expected, with the full concentration being recovered for objects that are approximately five times the system spatial resolution or larger. The recovery coefficient experiments were performed using cylinders of varying diameter, as opposed to other geometric shapes such as spheres. Although volumes of interest inside the patient may be more spherical than cylindrical, the use of cylinders to derive the recovery coefficient for a given diameter was more precise in that exact spherical diameters can be difficult to measure.

The fit of the paralyzable–non-paralyzable dead time model to the measured dead time data with an R^2 -value of 1.0 indicates the accuracy of the model that describes the relationship between the observed and true count rates. The deviation from the linear trend at high count rates is as expected, and suggests that dead time effects will only play a significant role at observed count rates of 40 kcps or greater.

Testing of the complete quantitative method yielded a calculated total activity inside the mixed material phantom that was within 2% of the true activity. The measurement of the residual in cold spots produced results within 13% of the expected amount of zero. The increase in residual measurements with low-density materials (in particular, air) was in agreement with the literature. However, an additional iteration of the Chang attenuation correction algorithm was found to improve this result slightly. The artifacts in the method are directly due to the fact that the Chang method for attenuation correction involves multiplication of an attenuation correction map with reconstructed data. As such, the erroneous cold spot values are already present in the data due to the step of reconstruction without attenuation correction. Further work may suggest that an alternative attenuation correction method may prove to be more suitable, for example, an incorporation into the OSEM algorithm for geometric mean data, which includes attenuation correction in the reconstruction step itself. Using the quantitative technique to evaluate hot spots is expected to produce results with a similar accuracy, providing that suitable recovery coefficient factors are applied to the data where necessary. For example, a hot spot of a size equivalent to the system spatial resolution would be expected to produce a 30% underestimate of the true concentration, however, with the application of the appropriate recovery coefficient factor this value would be expected to be within 5% of the true concentration. The accuracy of the method is further demonstrated with the anthropomorphic phantom results, producing an average calculated concentration in the liver and cardiac chambers that were within 2% and 4% of the true concentrations, respectively. The fact that the estimated concentration of activity inside the cardiac chamber agrees closely with the true concentration also suggests the correct modeling of the system's spatial resolution and partial volume effect.

The average difference of -1% between the true and calculated injected activities for the clinical lung ventilation/perfusion studies not only demonstrates the accuracy of the quantitative procedure, but also its practicality for the use in the clinic. Differences in the table that are represented as a negative number correspond to an underestimate of the true activity by the quantitative procedure. Such differences may be attributed to extravasation, where a small amount of the calibrated injected dose leaks into the tissue of the patient's arm at the site of injection, a mistake that is not uncommon in this procedure, or to the presence of a small amount of free $[^{99m}\text{Tc}]\text{-TcO}_4^-$ in the injected dose. Table 1 contains only one result with an absolute difference that is larger than 4% , and since this is an underestimate, extravasation is a very plausible explanation.

The errors associated with each step of the quantitative procedure were evaluated separately. The contribution of each to the final uncertainty of the complete process was determined by considering the dominance of each parameter or processing stage, and evaluating their effects on the final counts in the corrected data. Uncertainty in the camera's sensitivity factor and in the measurement of the scatter fraction parameter β was concluded to be the largest contributing factor, as well as errors associated with the assumption of a single system spatial resolution when considering the partial volume effect. The uncertainty introduced by this quantitative method has been estimated as 5% . Taking this uncertainty into account for the calculations made in table 1, we find that all but one of the quantitative results are within the error of the true injected doses. Furthermore, the qualitative features of the corrected images did not appear to suffer from a significant increase in image noise which is often associated with convolution-subtraction techniques. The corrected images were considered to be of a standard suitable for clinical interpretation purposes, allowing this method to act as a diagnostic tool both qualitatively and quantitatively.

The addition of incorrect counts due to septal penetration has not been included in this quantitative method. Although a low-energy collimator is being used for the detection of 140 keV photons, septal penetration is not considered to be significant when imaging with ^{99m}Tc (reported by Philips Medical Systems as approximately 1.2%). However, for other isotopes, such as ^{123}I , septal penetration must be taken into account when estimating the scatter component of the image. Iida *et al* (1998) have demonstrated that the addition of a constant to the build-up function (4) is a suitable means to account for the higher degree of septal penetration that occurs with such an isotope. Such a method will be taken into account when expanding this quantitative procedure to include other isotopes.

5. Conclusion

A comprehensive quantitative method for ^{99m}Tc SPECT/CT has been developed and validated using experimental phantom data and patient data. The method relies on transmission data from an additional low-dose CT study, which has the further benefit of supplying complementary anatomical information. The CT data are also necessary to provide a means to measure the diameter of objects when partial volume effect corrections are needed. The method is suitable for use in the clinic and demonstrates high accuracy when applied to actual clinical data.

Quantitative methodology based on SPECT/CT is undergoing further validation in the clinical environment, and will be extended for use with other radionuclides to make it a suitable technique for obtaining accurate quantitative data from a wide variety of nuclear medicine clinical procedures.

References

- Axelsson B *et al* 1984 Subtraction of Compton-scattered photons in single-photon emission computerized tomography *J. Nucl. Med.* **25** 490–4
- Bailey D L 1998 A cascaded paralyzable/non-paralyzable signal model: I. Report, MRC Cyclotron Unit, Hammersmith Hospital, London
- Bailey D L *et al* 2007 Development of a cost-effective modular SPECT/CT scanner *Eur. J. Nucl. Med. Mol. Imaging* **34** 1415–26 (abstract)
- Bailey D L *et al* 1987 Improved SPECT using simultaneous emission and transmission tomography *J. Nucl. Med.* **28** 844–51
- Bailey D L *et al* 1988 Development of an iterative scatter correction technique for SPECT *Aust. N.Z. J. Med.* **18** 501 (abstract)
- Blankespoor S C *et al* 1996 Attenuation correction of SPECT using x-ray CT on an emission–transmission CT system: myocardial perfusion assessment *IEEE Trans. Nucl. Sci.* **43** 2263–74
- Bocher M *et al* 2000 Gamma camera-mounted anatomical x-ray tomography: technology, system characteristics and first images *Eur. J. Nucl. Med.* **27** 619–27
- Brown S *et al* 2008 Investigation of the relationship between linear attenuation coefficients and CT Hounsfield units using radionuclides for SPECT *Appl. Radiat. Isot.* (at press) doi:10.1016/j.apradiso.2008.01.002
- Buvat I *et al* 1994 Scatter correction in scintigraphy: the state of the art *Eur. J. Nucl. Med.* **21** 675–94
- Chang L T 1978 A method for attenuation correction in radionuclide computed tomography *IEEE Trans. Nucl. Sci.* **25** 638–43
- Cranley K *et al* 1980 Correction for deadtime losses in a gamma camera/data analysis system *Eur. J. Nucl. Med.* **5** 377–82
- Deloar H M *et al* 2004 Optimization of the width of the photopeak energy window in the TDCS technique for scatter correction in quantitative SPECT *IEEE Trans. Nucl. Sci.* **51** 625–30
- Hoffman E J *et al* 1979 Quantitation in positron emission computed tomography: 1. Effect of object size *J. Comput. Assist. Tomogr.* **3** 299–308
- Iida H *et al* 1998 Effects of scatter and attenuation correction on quantitative assessment of regional cerebral blood flow with SPECT *J. Nucl. Med.* **39** 181–9
- Kashiwagi T *et al* 2002 Correction of nonuniform attenuation and image fusion in SPECT imaging by means of separate x-ray CT *Ann. Nucl. Med.* **16** 255–61
- Kim K M *et al* 2003 Contribution of scatter and attenuation compensation to SPECT images of nonuniformly distributed brain activities *J. Nucl. Med.* **44** 512–9
- LaCroix K J *et al* 1994 Investigation of the use of x-ray CT images for attenuation compensation in SPECT *IEEE Trans. Nucl. Sci.* **41** 2793–9
- Larsson A *et al* 2003 A method for attenuation and scatter correction of brain SPECT based on computed tomography images *Nucl. Med. Commun.* **24** 411–20
- Ljungberg M and Strand S E 1990 Scatter and attenuation in SPECT using density maps and Monte Carlo simulated scatter functions *J. Nucl. Med.* **31** 1560–7
- Ljungberg M and Strand S E 1991 Attenuation and scatter correction in SPECT for sources in a nonhomogeneous object: a Monte Carlo study *J. Nucl. Med.* **32** 1278–84
- Manglos S H *et al* 1987 Nonisotropic attenuation in SPECT: phantom tests of quantitative effects and compensation techniques *J. Nucl. Med.* **28** 1584–91
- Meikle S R *et al* 1994 A transmission-dependent method for scatter correction in SPECT *J. Nucl. Med.* **35** 360–7
- Moore S C 1982 Attenuation compensation *Computed Emission Tomography* ed P J Ell and B L Holman (London: Oxford University Press) pp 339–60
- Msaki P *et al* 1987 Generalized scatter correction method in SPECT using point scatter distribution functions *J. Nucl. Med.* **28** 1861–9
- Msaki P *et al* 1993 The convolution scatter subtraction hypothesis and its validity domain in radioisotope imaging *Phys. Med. Biol.* **38** 1359–70
- Mukai T *et al* 1988 Scatter correction in SPECT using non-uniform attenuation data *Phys. Med. Biol.* **33** 1129–40
- Narita Y *et al* 1996 Monte Carlo and experimental evaluation of accuracy and noise properties of two scatter correction methods for SPECT *Phys. Med. Biol.* **41** 2481–96
- Roach P and Bailey D 2005 Combining anatomy and function: the future of medical imaging *Internal Med. J.* **35** 577–9 (abstract)
- Siegel J A *et al* 1984 Absolute left ventricular volume by an iterative build-up factor analysis of gated radionuclide images *Radiology* **151** 477–81
- Thomas M D R *et al* 2005 A dual modality approach to quantitative quality control in emission tomography *Phys. Med. Biol.* **50** N187–94

- Vandervoort E *et al* 2007 Implementation of an iterative scatter correction, the influence of attenuation map quality and their effect on absolute quantitation in SPECT *Phys. Med. Biol.* **52** 1527–45
- Vines D C *et al* 2003 Evaluation of 2 scatter correction methods using a striatal phantom for quantitative brain SPECT *J. Nucl. Med. Technol.* **31** 157–60
- Wu R K and Siegel J A 1984 Absolute quantitation of radioactivity using the buildup factor *Med. Phys.* **11** 189–92
- Zaidi H and Hasegawa B H 2003 Determination of the attenuation map in emission tomography *J. Nucl. Med.* **44** 291–315